How to observe the small-scale spatial distribution of surface solar irradiance, and how is it influenced by cumulus clouds?

Zili He[1], Quentin Libois[1], Najda Villefranque[1], Hartwig Deneke[2], Jonas Witthuhn[2], and Fleur Couvreux[1]

[1]CNRM, Université de Toulouse, Meteo-France, CNRS, Toulouse, France
[2]Department: Remote Sensing of Atmospheric Processes, Leibniz Institute for Tropospheric Research, Leipzig, Germany

Correspondence: Quentin Libois (quentin.libois@meteo.fr)

Abstract. The amount of solar radiation reaching the Earth surface (SSI) is critical for a variety of applications, ranging from surface-atmosphere interactions to solar energy. SSI is characterized by a large spatiotemporal variability, in particular in the presence of broken clouds. This results in complex spatial patterns of shadows and sunlight directly related to clouds' geometry and physical properties. Although key in many respects, the instantaneous spatial distribution of SSI remains largely unexplored. Here, we use unique observations from a dense network of pyranometers deployed during the HOPE field campaign to investigate the SSI spatial distribution. For cumulus scenes, bimodal distributions are found, with one mode corresponding to cloud shadows and the other to sunlit areas with enhanced SSI exceeding clear-sky values. Combining large-eddy simulations of cumulus clouds with Monte Carlo ray tracing, we demonstrate the capability of advanced numerical tools to reproduce the observed distributions and quantify the impact of cloud geometrical and physical properties on both modes. In particular, cloud cover strongly modulates their amplitudes, in addition to their location and width, which are also sensitive to cloud height, geometrical depth, and liquid water content. Combining observations and simulations, we propose sampling strategies to estimate the instantaneous spatial distribution of SSI with a limited number of sensors, highlighting that 10 pyranometers integrated over 10 min can capture most details of the full distribution. Such a strategy could be used for future campaigns to further investigate SSI distributions and their impact on land-atmosphere exchanges or PV farm management.

1 Introduction

The amount of solar radiation reaching the Earth surface (hereafter referred to as SSI for surface solar irradiance) can be very variable in space and time, especially under broken cloud conditions (Long et al., 2006; Berg et al., 2011). In such conditions, SSI can even exceed clear-sky values when the sun remains visible in between clouds due to reflection by the cloud sides, a process often reported as cloud enhancement (Emck and Richter, 2008; Yordanov et al., 2012; de Andrade and Tiba, 2016). Although ubiquitous and very well known in the solar energy community (Lappalainen and Kleissl, 2020), this cloud enhancement has not been much investigated in the atmospheric science community because it generally vanishes with spatial and temporal averaging on scales relevant to energetic transfers in the Earth system. This phenomenon, and more generally all radiative processes implying horizontal transfers in the presence of clouds, sometimes called 3D radiative effects of clouds, also remain overlooked in the atmospheric radiative transfer modelling community because most radiative transfer models

1

25 embedded in atmospheric models rely on the plane parallel hypothesis, which inherently precludes to simulate such features (Várnai and Davies, 1999; Villefranque and Hogan, 2021). However, the spatial heterogeneity of SSI under broken cloud conditions is critical for the surface energy budget and land-atmosphere interactions (Lohou and Patton, 2014), the development of small-scale convection (Jakub and Mayer, 2017; Veerman et al., 2022), as well as for the stability of electrical systems fed by solar energy (Alam et al., 2014; Lohmann et al., 2016; Lohmann, 2018) or for urban thermal studies (Pacifici et al., 2019;

30 Sanchez et al., 2021). As an illustration, the production of PV panels is very local, and the management of a PV plant is sensitive to small-scale irradiance variations because the time response of a PV system is nearly instantaneous (Gueymard, 2017). Although the complexity of the SSI spatial distribution is currently uncaptured by standard atmospheric models, the need from various sectors to better anticipate the detailed impact of clouds on SSI is now challenging the atmospheric science community.

35 While the instantaneous SSI spatial distribution is key for many applications, it remains difficult to assess. Standard SSI measurements are generally punctual and can only capture local temporal variations so that fast temporal variations are much more documented than small-scale spatial gradients (Inman et al., 2016). Satellite observations can provide a two-dimensional view of the Earth surface, but the spatial resolution of SSI satellite products is generally coarse compared to that of individual clouds, and estimating SSI from above requires many assumptions (Qu et al., 2017). Moreover, standard retrieval algorithms

40 cannot capture cloud enhancement (Huang et al., 2019), making such products inadequate to investigate the details of SSI spatial distribution (Beyer, 2016). As a result, most we know about SSI spatial variability comes from modelling. For decades, large-eddy simulations (LES) have been used to simulate cloud fields (Brown et al., 2002; Siebesma et al., 2003), and they now allow the simulation of extremely realistic clouds (Villefranque et al., 2019). These clouds have been extensively evaluated in terms of their geometrical and physical properties, often based on comparisons between spatial averages over the LES

45 domain and vertical profiles observations (Neggers et al., 2003; Oue et al., 2016; Endo et al., 2019), but much less in terms of their radiative impact. Assessing SSI fields would be a stringent test for the LES simulations, as such fields are sensitive to all geometrical and physical details of the simulated clouds. It is only recently that a few studies have carefully looked at SSI fields by combining LES with online or offline 3D radiative transfer models (Jakub and Mayer, 2017; Gristey et al., 2020b; Veerman et al., 2022). Gristey et al. (2020a) showed, for instance, that the features of the SSI spatial distribution under cumulus clouds

50 are directly related to the macroscopic organization and physical properties of the clouds. This is a promising venue to better characterize these clouds, which are particularly difficult to observe from space due to their small size. Tijhuis et al. (2023) proposed a method to reconstruct realistic SSI spatial distributions from plane parallel simulations. To this end, they applied a Gaussian filter to the SSI fields obtained under the plane-parallel hypothesis, allowing cloudy diffuse radiation to artificially spread over directly illuminated areas, somehow mimicking 3D effects. Yet, so far, the observational equivalent of such SSI

55 spatial distributions is still largely missing, although a few field campaigns have already investigated related questions.

For instance, a network of 17 pyranometers was deployed around Kalaeloa airport on Oahu, Hawaii, from March 2010 to October 2011 (Sengupta and Andreas, 2010). This network has been used to investigate the power spectra of irradiance time series for individual sensors and for their average (Tabar et al., 2014) and to extract 2D fields of cloud motion vectors from ground-based observations of cloud shadows (Weigl et al., 2012). Luger et al. (2013) also used a grid of irradiance sensors to

estimate the SSI spatial distribution on a PV farm and extract cloud velocity vectors. The HOPE field campaign (Macke et al., 2017), which took place in 2013 around Jülich, Germany, focused on the small-scale interactions between the surface and the atmosphere, in particular for the evaluation of subgrid processes in atmospheric models. During the campaign, an original instrumental system comprising 99 pyranometers was deployed for the first time (Madhavan et al., 2016). These observations have been carefully analyzed by Madhavan et al. (2017), with a main focus on the correlations between observations made by different sensors. These authors primarily aimed at quantifying the representativity of a single sensor for a neighbouring area. In particular, they showed that correlations arise at different spatial scales depending on the cloud regime. However, they did not focus much on the instantaneous SSI spatial distributions. Using the same dataset, Lohmann et al. (2016) also focused on the correlations between time series to better predict local changes of SSI but did not look at the spatial distributions either. Yet, this dataset is promising for investigating, from an observational point of view, the spatial variability of SSI. More recently, Mol et al. (2023) used a dense network of 20 to 25 radiometers to investigate the impact of clouds on SSI spatial patterns, focusing in particular on the spectral dimension of SSI. Other studies attempted to construct spatial fields of SSI, for instance, using a network of sky-imagers to locate clouds in the sky and then project their shadows at the surface (Nouri et al., 2022). However, in such cases, clouds are attributed an average transmissivity (Nouri et al., 2019) that does not capture the complexity of the radiation field in and around the cloud shadows. Kuhn et al. (2017) alternatively used a shadow camera to estimate SSI fields with an accuracy of about 10 % but did not discuss how the measurement errors modified the overall distribution.

With the existing literature on SSI spatial variability in mind, the main objective of the present study is to accurately assess instantaneous SSI spatial distributions under cumulus clouds from an observational perspective using the HOPE dataset. We focus on cumulus clouds because the associated variability is supposedly the largest and because these clouds, ubiquitous across a large fraction of the globe, remain a challenge for weather and climate modelling. A secondary objective is to propose measurement strategies to capture the SSI spatial distribution with a limited network of radiation sensors, which is addressed by combining the observations and LES simulations. Eventually, we aim to understand which cloud properties control SSI spatial distributions. To this end, we first develop a method to identify situations from the HOPE dataset corresponding to golden cases of cumulus clouds, i.e., very homogeneous fields close to those simulated by ideal LES. Then we compare the SSI spatial distributions from one situation to the other, along with a reference simulation performed with an LES coupled to a 3D radiative transfer code. This simulation system is further used to perturb the cloud properties in the model and see how it impacts the SSI fields.

Section 2 introduces the HOPE dataset, the LES model and the simulations, as well as the 3D Monte Carlo radiative transfer code. The methodology followed to answer the objectives of this study is then detailed in Sect. 3. The analysis of the SSI spatial distributions from both the observations and reference simulations are presented in Sect. 4, while Sect. 5 further investigates how instantaneous SSI spatial distributions can be approached by appropriate spatiotemporal sampling of SSI. Finally, sensitivity tests are performed in Sect. 6 to investigate the impact of cloud properties on the SSI fields. Section 7 summarizes the main results and gives some perspectives.
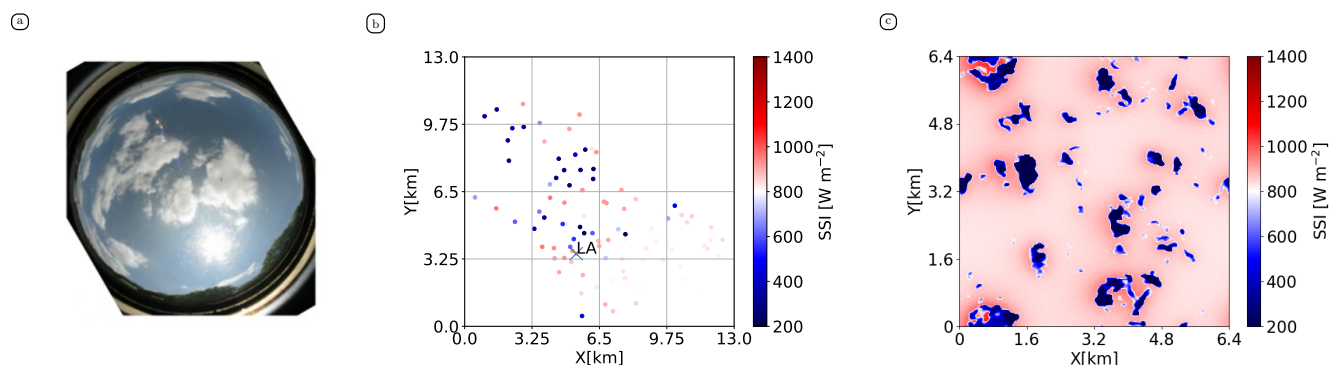
Figure 1. Illustrations of data used in this study. (a) All-sky image at 10:37:30 UTC on 5 May 2013. The picture was taken at LACROS station, which is marked as "LA" in (b). (b) Mean SSI over one minute, measured by the 99 pyranometers from 10:37 to 10:38 UTC on 5 May 2013. (c) Simulated SSI under a synthetic cumulus cloud field simulated by a Meso-NH LES under the same solar zenith angle as in (b).

2 Data

2.1 Observations from the HOPE field campaign

95   The High Definition Clouds and Precipitation for advancing Climate Prediction (HD(CP)2) Observational Prototype Experiment (HOPE) campaign (Macke et al., 2017) was designed to evaluate the German community atmospheric model (ICON) and to learn about atmospheric physics at spatiotemporal scales at which processes are parameterized in the model. To this end, observations of aerosols, clouds, and precipitation were collected with high spatial and temporal resolutions near Jülich, Germany (50.909°N, 6.4139°E, 111 m asl) in April and May 2013.

100   During this campaign, and until July 2013, a high-density network of 99 pyranometers was deployed (although some of them have not been working all the time) on a 10×12 km^2 area (Madhavan et al., 2017). The SSI (i.e. the downwelling solar flux density per unit of horizontal surface in W m^{-2}) was measured at 10 Hz and then averaged at 1 Hz. The low-cost silicon sensors used are only sensitive across the spectral range of 300-1100 nm, hence SSI retrieval requires a calibration step. As the spectral distribution of SSI varies depending on atmospheric conditions (Lindsay et al., 2020), this calibration can result in

105   errors up to 5%.

In addition to these pyranometers, the Leipzig Aerosol and Cloud Remote Observations System (LACROS) station was deployed at Krauthausen (50.880°N, 6.415°E, 99 m asl) in April and May, the two-month period on which we focus in this study. The station includes a 35-GHz cloud radar and a lidar ceilometer, from which cloud boundaries (cloud base and top heights) can be retrieved, a microwave radiometer measuring liquid water path (LWP, in kg m^{-2}), as well as an all-sky imager

110   (Bühl et al., 2013).

Figure 1 shows a sample of this dataset on a day with fair-weather cumulus clouds, as can be seen on the image captured by the all-sky imager (Fig. 1(a). Figure 1(b) shows the instantaneous SSI measured by the pyranometer network. Small SSI values

around 500 W m^{-2} (blue points) correspond to cloud shadows, while large values closer to 1000 W m^{-2} (red points) correspond
to clear sky. It can be noticed that clear-sky values are far from homogeneous in space, a point that will be specifically addressed
115   later.

2.2   Large-eddy simulations

To complement the HOPE observations, a high-resolution simulation of a golden case of developing cumuli over land, namely
the ARM cumulus case (Brown et al., 2002), is used. The simulation is run with the Meso-NH model (Lac et al., 2018) for
15 hours over a 6.4 km wide (domain size similar to the area covered by the pyranometer network) and 4 km high periodic
120   domain with horizontal and vertical resolutions of 25 m. Three-dimensional fields of liquid water content (LWC), specific
humidity, temperature, pressure, and wind are output every minute during the cloudy hours of the simulation. The model uses
an anelastic system of equations and a 3D turbulent kinetic energy scheme (Cuxart et al., 2000) with a diagnostic mixing
length (Deardorff, 1980). For the advection of meteorological and scalar variables, discretization of the spatial derivative is
based on a piecewise parabolic method, enabling the scheme to handle sharp gradients and discontinuities very accurately.
125   Time integration is forward-in-time. Advection of momentum is solved using a centred discretization of the fourth order in
space and a Runge-Kutta-centered fourth-order scheme in time. The water phase transformations are parameterized with the
ICE3 one-moment microphysical scheme (Pinty and Jabouille, 1998). Diurnally varying surface turbulent fluxes are prescribed
during the simulation, as well as cooling and drying tendencies summarizing large-scale advection and radiative tendencies as
described in Brown et al. (2002).

2.3   Radiative transfer simulations

A 3D radiative transfer model based on Monte Carlo methods (Villefranque et al., 2019) is used to simulate SSI fields every
minute of the fifth hour of the LES (10:30-11:30 LT) in offline mode. It uses the solar zenith angles (SZA) at Jülich on 5
May 2013, from 11:36 to 12:36 UTC, which decreases from 36.8 to 34.5°. Each pixel of each field is a 5×5 m^2 square.
To each pixel corresponds an SSI estimate, calculated as the mean flux over 15000 photon-path realizations, resulting in a
135   statistical uncertainty of approximately 1%. An example of such a field is presented in Fig. 1(c). Three-dimensional fields of
LWC and water vapour are used to describe extinction in the LES domain, which is periodically repeated on the horizontal.
The standard mid-latitude summer atmospheric profile, also used in the I3RC cumulus case (Cahalan et al., 2005), is used
as background atmosphere above the domain. Gaseous absorption properties are computed for this background atmosphere
using the correlated-k model implemented in RRTMG (Iacono et al., 2008) and for twenty profiles with perturbed absorption
140   coefficients. These pre-tabulated absorption coefficients are then interpolated to account for the actually simulated water vapour
concentrations in the LES domain (see Appendix C.2.1 of Villefranque et al., 2019). Cloud droplets have a constant effective
radius of 10 μm and an effective variance of 0.010. Their optical properties are computed from Mie calculations using the code
developed by (Mishchenko et al., 2002) and assuming log-normal size distribution. The surface is assumed Lambertian with
the spectral albedo of grass (Meso-Star, 2021). To simulate broadband solar fluxes, spectral integration is performed from 0.3
145   to 4 μm.

3 Methods

3.1 Objective selection of cumulus cloud periods

As this study focuses on cumulus clouds, cumulus scenes need to be identified from the observations. In order to select one-hour-long periods when cumulus are present, four metrics are defined:

$$c_1(t) = \langle \langle \mathrm{CSI}(x,t) \rangle_x \rangle_t, \tag{1}$$

$$c_2(t) = \langle \sigma_x \left[\mathrm{CSI}(x,t) \right] \rangle_t, \tag{2}$$

$$c_3(t) = \sigma_t \left[\langle \mathrm{CSI}(x,t) \rangle_x \right], \tag{3}$$

$$c_4(t) = \sigma_x \left[\langle \mathrm{CSI}(x,t) \rangle_t \right], \tag{4}$$

where $\mathrm{CSI}(x,t)$ is the clear-sky index at location x and time t, defined as $\mathrm{CSI} = \mathrm{SSI}/\mathrm{SSI_{cs}}$ (Lohmann and Monahan, 2018), with $\mathrm{SSI_{cs}}$ the theoretical clear-sky SSI estimated from a clear-sky model (Ineichen, 2008, 2016) embedded in the *pvlib* python package (Holmgren et al., 2018). This model accounts for climatological concentrations of aerosols, ozone, and water vapour. Yet, local conditions at the moment of the measurement might significantly differ from their climatologies, hence the CSI might be biased. However, this should not affect the identification of the cumulus cloud periods. $\langle . \rangle_u$ and $\sigma_u \left[. \right]$ denote average and standard deviation, respectively, taken over dimension u. Spatial dimension ($u = x$) implies that data are taken over all pyranometers, and temporal dimension ($u = t$) implies that data are taken over one hour centered on t.

c_1 and c_2 thus quantify the temporal average of the spatial mean and spatial variability of CSI, respectively. Hence large values of c_1 indicate situations where either no clouds are present, or they are present with a minor effect on radiation on average. It means that either their fractional cover or their optical depth is small. Combined with large values of c_2, which indicate high spatial variability of CSI, broken cloud situations can be detected and clear-sky or homogeneous optically thin clouds eliminated. c_3 quantifies the temporal variability of the averaged SSI over the domain, which allows the identification of stationary situations. Eventually, c_4 quantifies the spatial variability of the averaged SSI over the time period, which allows the selection of statistically uniform cloudy situations over the domain. Figure 2(a)-(b) shows the time series of the four metrics for selected periods in April and May.

To identify periods with broken cloud conditions, we follow a two-step process:

- Pre-selection based on c_1 and c_2: from our data, we identify periods where c_1 and c_2 are among the highest. Specifically, we look for the periods that fall within the top 30% for both c_1 and c_2 to focus on times when broken clouds are present. The selected periods are highlighted by red dots in Fig. 2.

- Complementary selection using c_3 and c_4: among these pre-selected periods, we apply another filter based on two additional criteria, such that c_3 and c_4 values are both among the lowest 30% of the pre-selected cases. This step helps refine the selection to periods where cumulus fields are temporally stable and spatially uniform.

After these two steps, five cases are identified and highlighted by red vertical lines in Fig. 2(a)-(b), on April 18th, April 20th, April 25th and May 5th (2 periods). Thanks to the all-sky images, it was verified that they indeed correspond to cumulus cloud situations, thereby validating our automatic selection procedure.

Figure 2(c) zooms on the selected periods and shows as well the metrics computed from the LES cumulus cloud field (where clear-sky SSI is estimated from a clear-sky radiative transfer simulation using the same Monte Carlo code and setting LWC to zero). The metrics c_1, c_2 and c_3 are very similar between the observations and the simulation. On the contrary, c_4 is significantly smaller in the simulation than in the observations, which suggests that the real situations still feature more spatial heterogeneity than the ideal case characterized by a uniform surface and periodic boundary conditions.

Figure 2(d) shows the values of the four metrics for several days identified as "broken clouds" by (Madhavan et al., 2017). The only intersection between their set of broken-cloud cases and ours is April 25th. Note, however, that Madhavan et al. (2017) selected entire days, whereas we selected only hours. Cases we selected might occur during days otherwise clear or overcast, hence not considered as broken-cloud days. It is puzzling, though, that we did not select more cases on days flagged as cumulus days by Madhavan et al. (2017). Looking at our metrics during these days, one can see that they are indeed characterized by high c_2 values, suggesting a spatially heterogeneous SSI, but considerably lower c_1 values than in our selected cases, suggesting larger cloud covers or optically thicker clouds. Furthermore, they are associated with larger c_3 and c_4 values, suggesting the periods are less temporally and spatially stable compared to the periods we identified in this work. This might indicate that our criteria are too restrictive. Note that actually, our method was designed to identify cumulus periods, but not necessarily all of them. In particular, the condition on c_1 could have been less strict. It is also possible that normalized standard deviation (divided by mean values) would have been more adapted than absolute standard deviations for c_3 and c_4. The selection procedure could thus certainly be refined for future studies. However, for the present study, we will use the 5 selected cases highlighted in Fig. 2(c).

3.2 SSI distributions

To characterize the SSI spatial distribution, probability density functions (pdfs) of normalized SSI are used, in line with Gristey et al. (2020b). The normalization factor is simply the cosine of SZA at the time and location of measurement in the case of observations or of prescribed SZA in radiative transfer simulations in the case of LES data (in which case SZA values correspond to those of P5). Hereafter these pdfs are simply referred to as SSI distributions. Except when stated otherwise, the SSI distributions are constructed by cumulating data at one-minute resolution during one hour (which implies 1-minute averages for the observations) and over the whole domain (99 pyranometers in the observational dataset, 1280×1280 grid points in the LES data). Bins are 30 W m^{-2} wide.

The distributions are bimodal, with one mode corresponding to cloud shadows and the other to clear sky (inter-shadows gaps). It can be seen in Fig. 1(b)-(c) that the largest values correspond to clear-sky regions near cloud shadows being over-illuminated. Indeed, these regions receive additional radiation reflected by cloud sides, a 3D effect sometimes called enhancement, side leakage, or channelling, and well documented in the literature (e.g. Marshak and Davis, 2005).
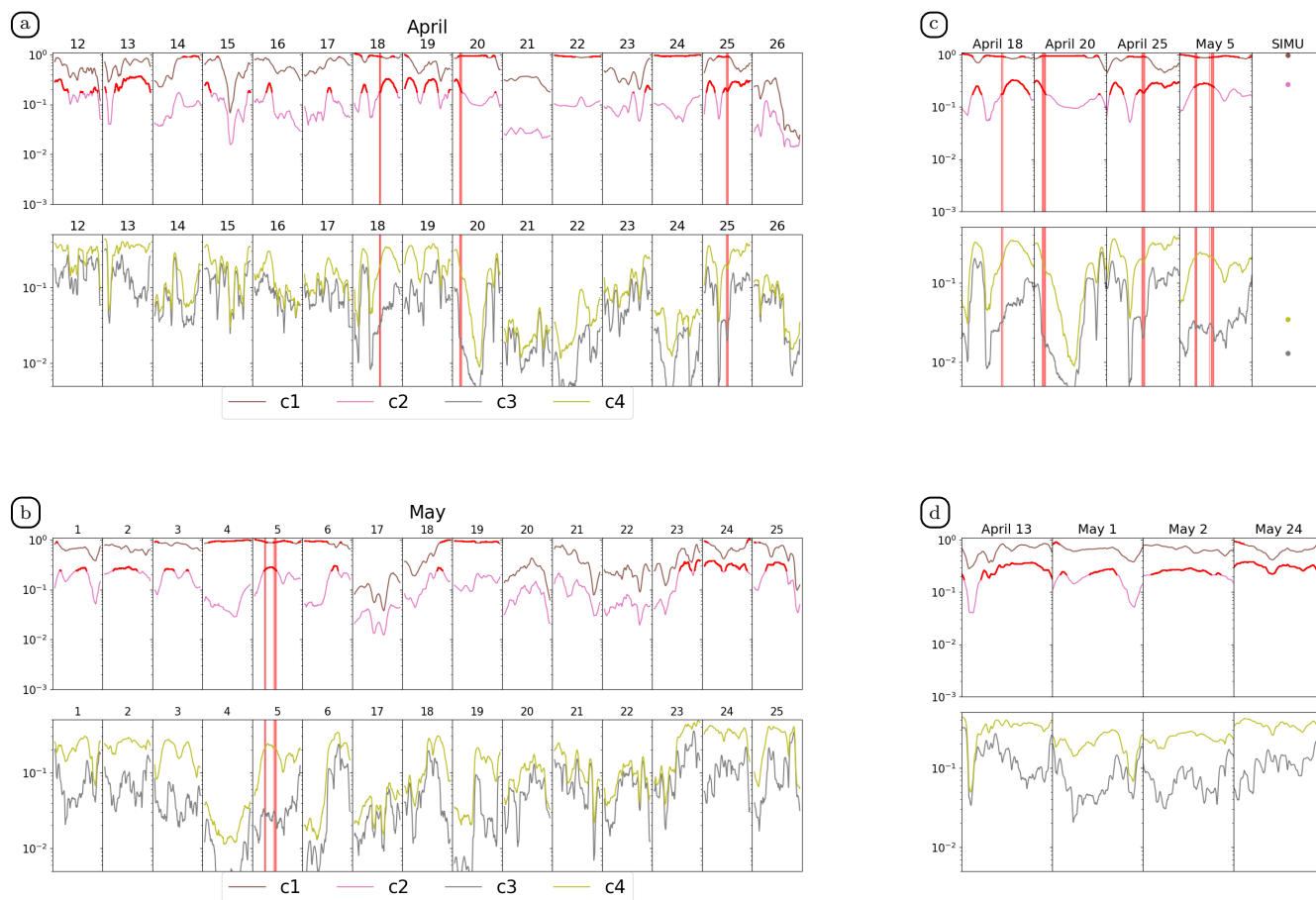
Figure 2. Time series of the four metrics c_i in (a) April and (b) May. Values of the four metrics for (c) the periods identified as cumulus cloud hours following our method (highlighted by red vertical lines) and the simulation, and (d) for the periods identified as cumulus cloud days by Madhavan et al. (2017).

Gristey et al. (2020a) used a neural network trained on LES data to show that the parameters of analytical functions matching
210 each mode of the SSI distribution could be predicted from a few properties describing the cloud field. This implies that these
distributions contain valuable information on the overlying cloud field. In the following, the distributions are characterized by
the mean and standard deviation of subsamples corresponding to each mode without assuming particular distribution shapes.
This is a way to condense the information and facilitate its interpretation. The cloud-shadow mode corresponds to values
smaller than 500 W m^{-2}, whereas the clear-sky mode corresponds to values larger than 900 W m^{-2}. Values in between corre-
215 spond to shadow edges. They are associated with low relative occurrence and are excluded from the analysis. To compare two
distributions obtained from different cloud fields or different datasets, root mean square deviations (RMSD) will be computed
on the whole histogram and on each mode separately.

3.3 Modification of LES fields

Sensitivity tests are performed in Sect. 6 in order to better understand how cloud characteristics drive SSI distributions. For
220 each category of test, the 60 LES cloud fields of the one-hour-long simulation are modified, varying cloud LWC, cloud base
height, cloud depth, or cloud fraction, with the objective of changing one property of the cloud field at a time and preserving
all the others to isolate its influence. The various categories of tests are:

- `LWCx`, where LWC in the clouds is uniformly scaled by a given factor (e.g., 0.6 or 1.4);

- ΔH, where the full cloud layer is translated on the vertical (e.g., 400 m closer to the surface (Δ H =-400) or 400 m higher
225 (Δ H =400));

- ΔD, where cloud layer depth (D) is increased. First, each cloudy column is shifted upwards by n layers of thickness Δz
(in the following, $n = 16$ and $\Delta z = 25$ m); that is, clouds are moved upwards by a distance $n\Delta z$. Then, n layers below
new cloud base are filled with the same LWC as the original cloud-base layer. Finally, LWC is scaled column-wise so
that the LWP field is unchanged: the whole field contains the same total mass of liquid water as the original one, but the
230 maximum LWC is smaller;

- `CC`, where cloud fraction at each layer (and thereby the total cloud cover (CC) seen from above as well), is increased.
To this end a collection of translated cloud fields is first created by incrementally shifting the original cloud field in
each horizontal direction (including diagonals), up to a given distance (e.g. 125 m). Then, the resulting translated cloud
fields are averaged together. Finally, the resulting 3D field of LWC is uniformly scaled at each vertical level so that the
235 original "in-cloud" LWC (defined in each model layer as horizontal domain average content divided by cloud fraction),
is unchanged.

In sensitivity tests `LWCx` and ΔH, the impacts of changing LWC and cloud base height are well isolated. In ΔD and `CC`,
however, not only is the cloud geometry modified, but also the LWC distribution inside clouds and across the domain. In ΔD,
LWP is preserved, but the shape and absolute values of LWC vertical profiles are modified. This might result in unrealistic
240 features in clouds, hence in SSI fields. In `CC`, layer-wise mean in-cloud LWC is preserved, but as cloud fraction increases,

Table 1. Cloud properties resulting from the sensitivity tests. Each property is given at the first/last timestep of the one-hour-long period. Symbol — indicates the same value as control.

Case	cloud base height	cloud layer depth	liquid water path	max water content	cloud cover
(units)	(m)	(m)	(g m^{-2})	(mg kg^{-1})	(%)
Control	825 / 875	350 / 700	1.6 / 9.4	9.7 / 34.0	14.3 / 27.7
LWCx0.6	—	—	0.9 / 5.6	5.8 / 20.4	—
LWCx1.4	—	—	2.2 / 13.1	13.6 / 47.5	—
ΔH=-400	425 / 475	—	—	—	—
ΔH=400	1225 / 1275	—	—	—	—
ΔD=400	—	750 / 1100	—	6.0 / 26.7	—
CC=125	—	—	6.7 / 30.8	41.4 / 105.3	46.2 / 59.8

the total amount of water in the domain also increases. Table 1 summarizes the various tests performed and the corresponding modifications of the cloud field.

4 SSI distributions in observations and simulations

Five cumulus periods of 1 hour were selected in the observations following the method detailed in Sect. 3.1. Figure 3(a) shows

245 the SSI distributions for each period. For each case, an effective cloud cover is diagnosed by computing the fraction of the measurements (99 pyranometers during one hour), with normalized SSI lower than 900 W m^{-2}. This is referred to as "shadow cover" in opposition to the "cloud cover" classically defined as the fraction of a domain covered by clouds when seen from above. Figure 3(a) also shows a SSI pdf for a clear-sky period, taken on 4 May 2013, 12:12-12:13 UTC, which was also flagged as clear sky by Madhavan et al. (2017) and confirmed by all-sky images.

250 Looking at SSI distributions in the presence of broken clouds, one can see that all cases are characterized by similar bimodal distributions. Their properties differ between the various observed cases, although one interesting common feature, already pointed out by Gristey et al. (2020b), is that a large number of values are significantly larger than the values expected in clear-sky conditions — a typical signature of 3D radiative effects. In a sense, clouds act like the mirrors that are used to collect solar radiation in concentrated solar power systems. Interestingly, based on the shadow cover values, it seems that maximum cloud

255 enhancement tends to increase with cloud cover.

Figure 3(b) presents simulated and observed distributions under clear-sky conditions. They are both unimodal and symmetric, with approximately the same width and around the same mean value. However, it is important to note that their widths have distinct origins. The observed distribution results from instrumental, intrinsic variability, as well as heterogeneity in atmospheric (e.g. water vapour, aerosols) and surface (e.g. albedo), whereas variability in the simulations is dominated by Monte

260 Carlo statistical noise. Both simulations and observations account for water vapour heterogeneity, but its effect on solar radiation is too small to explain the obtained standard deviations. Increasing the number of photons in the Monte Carlo simulation
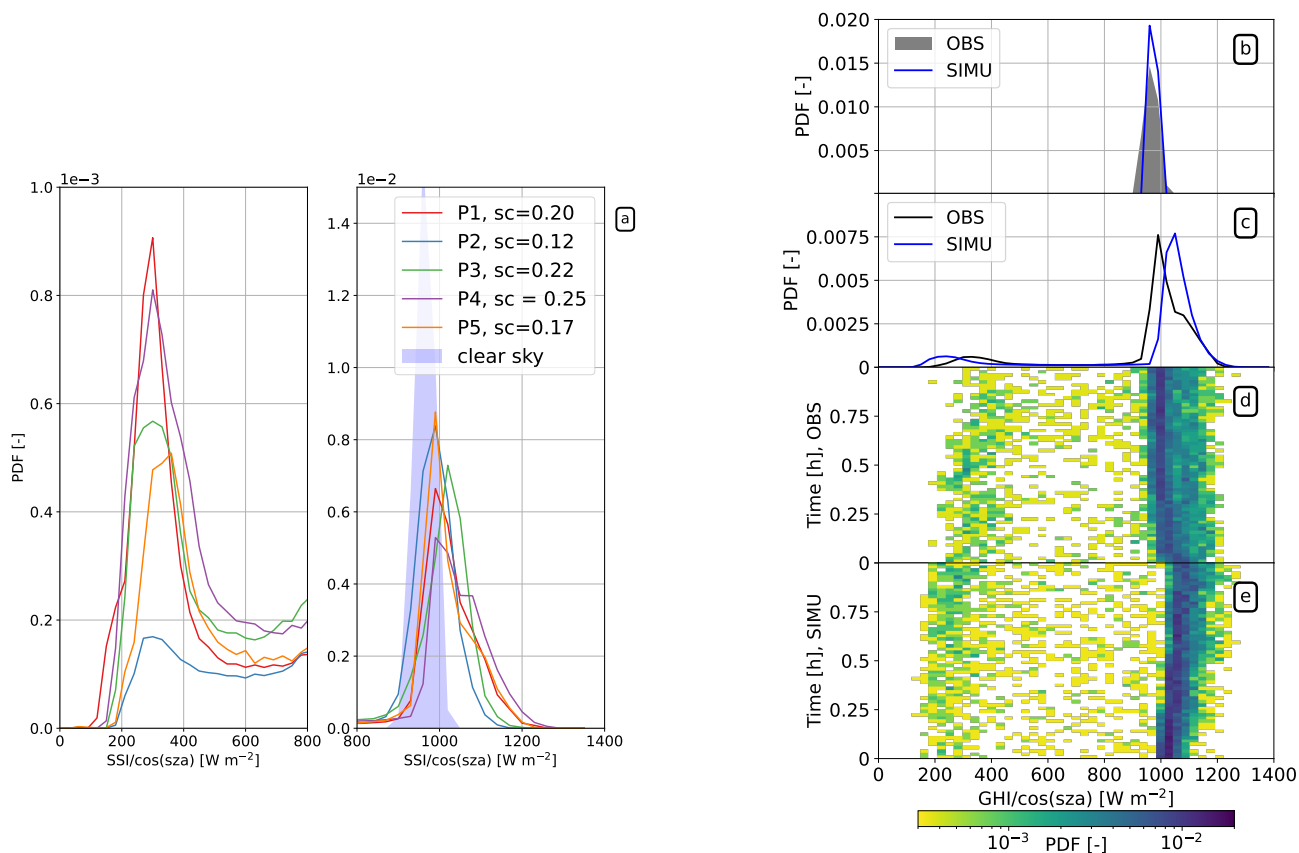
Figure 3. Observed and simulated normalized SSI distributions. (a) Distributions for the 5 selected periods in UTC: P1: 18 April 2013, 13:00-14:00; P2: 20 April 2013, 9:12-10:12; P3: 25 May 2013, 12:32-13:32; P4: 5 May 2013, 9:30-10:30; P5: 5 May 2013, 11:36-12:36. sc in the legend indicates the "shadow cover", which corresponds to the fraction of the surface occupied by cloud shadows (integration of the distribution from 0 to 900 W m^{-2}). The pdf for a clear-sky period (4 May 2013, 12:12-12:13 UTC) is also shown. (b) Observed (P5) and (c) simulated distributions of the SSI as a function of time along the one-hour period. (d) Distributions of observed (same as panel a) and simulated SSI during a clear-sky period of 1 minute. (e) Distributions of observed (P5) and simulated SSI Cumulated over the full hour.

leads to a narrower distribution (not shown). Hence it is a coincidence that both sources of noise have the same amplitude here: the inherent lack of heterogeneity in the LES is somehow balanced to the right amount by Monte Carlo noise. Because these noises introduce much less variability than that caused by the presence and characteristics of clouds, in the remaining parts of

265   this study, both simulations and observations are analyzed without further consideration of noise. Nevertheless, the detailed understanding of the observed clear-sky pdfs certainly deserves more attention to disentangle the sensor's inter-calibration issues from the actual spatial variability of SSI across the observed domain.

Figure 3(c) compares the observed (P5) and simulated SSI distributions cumulated over the full hour. As for P5, only 95 are used (four were not working during this specific period), and only 95 pixels were randomly sampled in the simulation

270   for fair comparison. The distributions have very similar shapes, although the observed one shows a bump in the right part of the clear-sky mode that is not present in the simulated one. The cloud-shadow mode is also shifted towards lower values in the simulation compared to the observations, while the simulated clear-sky mode peaks at a greater normalized SSI than the observed one.

To further understand the cumulated distributions, Figures 3(d) and e show the SSI distributions for each minute of P5 and of

275   the simulation. It is clear that the shape of the distributions is relatively constant throughout the hour. It can be seen, however, that the cloud cover (integral of the cloud-shadow mode) increases along the simulation, as already noticed in Table 1. This seems in turn to increase 3D effects and therefore, amplify enhancement of SSI in clear-sky regions between cloud shadows, as suggested by the shift towards larger values of the clear-sky peak. In the observations, the clear-sky mode appears quite stationary, apart from the very beginning, which features larger values and probably explains the bump of the cumulated

280   distribution (Fig. 3(c)). On the contrary, the cloud-shadow mode shifts to larger values with time, which could suggest that clouds are getting optically thinner or that light entrapment between the surface and the clouds is getting more intense (Hogan et al., 2019; Villefranque et al., 2023). It can also be noticed that small SSI values (that is, inside cloud shadows) are consistently smaller in the simulation than in observations, meaning that the observed and simulated cloud fields are probably distinct in terms of detailed cloud physical properties.

285   A detailed investigation would be needed to further understand all these differences, in particular, to disentangle the role of assumptions made in the LES and radiation code (idealized surface, limited area domain with periodic boundary conditions, approximate scattering phase function for cloud droplets, arbitrary and homogeneous value of the cloud droplet effective radius...) from the role of actual differences of cloud properties and geometry. This is out of scope here, as we only aimed to demonstrate that the combination of LES and Monte Carlo numerical tools is well suited to simulate realistic SSI distributions.

290   To have a better match between observations and simulations, simulations should correspond to the same atmospheric and surface conditions as the observations, which is not the case here. Note that the LASSO experiment on the Atmospheric Radiation Measurements Southern Great Plain site was specially designed to allow strict comparison between observations and LES (Gustafson Jr et al., 2020) and would provide a very relevant framework to investigate these questions.

5   Sensitivity of SSI distributions to spatio-temporal sampling

295   We have shown in the previous section that cumulating SSI measurements from a dense network of 99 (or 95 in P5) pyra-
nometers over one hour allows us to capture most of the spatial variability of SSI. However, such instrumental configuration is
unique to the HOPE campaign and cannot be practically deployed in all field campaigns. Hence this section aims at providing
guidance on the measurement strategy needed to estimate instantaneous SSI distributions in the presence of broken clouds. To
this end, we analyze the sensitivity of the distributions to the number of pyranometers used to compute this distribution and to

300   the time period on which observations are cumulated. We apply the same strategy to the observations and simulations.

To gain insight into the way temporal and spatial sampling together operate, we first focus on the hourly distributions. Based
on the P5 observations, we assess the deterioration of the full distribution (95 pyranometers over one hour) induced by either
using fewer pyranometers or spanning a shorter period. Figure 4(a) shows the evolution of the RMSD between the approximate
and the full distributions for various numbers of pyranometers and periods of integration (all symmetrical around the middle

305   of the full period). For each period of integration, the subsampling is repeated for 512 different random combinations of the
same number of pyranometers to measure the uncertainty of the results. As expected, decreasing the number of measurement
sites or the duration of integration increases the RMSD. The sensitivity to the time period seems quite independent of the
number of pyranometers, as suggested by the fact that the curves are almost parallel to each other in Fig. 4(a). The individual
contributions of the cloud-shadow and clear-sky modes are shown in Fig. 4(b), with a dominant contribution from the clear sky

310   (expected from the larger values). When setting the integration period to 10 min, a time scale at which the cloud field can be
considered stationary, at least 50 pyranometers over the 10×12 km^2 are needed to reduce the RMSD down below 5×10^{-4},
which is the minimum value needed to distinguish distributions corresponding to distinct cloud geometrical characteristics
(see Sect. 6). In particular, we note a strong reduction of the clear-sky RMSD from 4.5×10^{-3} to 5×10^{-4}. Examples of
reconstructed distributions are shown in Fig. 4(c) and can be compared to the reference distribution represented by the pink

315   shading. It shows that the sensitivity of the reconstructed distributions to integration time is smaller than their sensitivity to
the number of sites and that 10 sites are essentially enough to capture the variability measured at all sites. A similar RMSD is
obtained when cumulating 5 pyranometers over 1 hour or 10 pyranometers over 10 min, or between 10 pyranometers over 1
hour and 50 pyranometers instantaneously.

The same analysis is now carried out for the simulation, where a larger number of measurement sites can be sampled

320   (Fig. 4(d)). Here, the reference distribution to compute the RMSD contains all 1280×1280 pixels of the simulation, cumu-
lated over one hour. Qualitatively, the sensitivity of RMSD to subsampling is similar to the observations, that is, the error
increases when either the number of measurement sites or the integration time is reduced. However, the decrease of RMSD
with integration time is much faster at shorter integration times in the simulation. This may be related to a stronger background
wind in the simulation (10 m s^{-1}) than in P5 (5 m s^{-1} at 1 km altitude as measured by radiosoundings). There is an inflexion

325   point around 600 s for the sensitivity to the integration time when a single measurement site is used (the time position of this
inflexion point decreases with the number of sites). According to the mean wind in the simulation and assuming that clouds do
not significantly evolve (Taylor hypothesis), this corresponds to a 5 km distance sampling. These tests suggest that the hourly

distribution is captured satisfactorily (RMSD below 5×10^{-4}) when using 50 pyranometers over 240 s or 10 pyranometers over 1200 s. The decomposition of the RMSD between the clear-sky and cloud-shadow modes is shown in Fig. 4(e). Interest-

330 ingly, clear-sky RMSD dominates for integration over less than 1000 s, while for larger integration times, both modes equally contribute. Figure 4(f) shows the various distributions for a given duration (600 s) or a given number of pyranometers (10). It confirms a stronger sensitivity to the number of measurement sites than to the integration time.

In the previous series of tests, sensitivity to integration time was explored, although when the hourly distribution of SSI is the target, there is no reason to integrate over a shorter period of time. However, when the instantaneous spatial distribution of SSI

335 is sought, temporal integration can become a solution to construct the full distribution, at least when the cloud field is advected horizontally by the wind. This finding implies that we can trade a high spatial density of observations for longer integration times. Figure 5 documents how combining temporal and spatial sampling in the simulation allows the reconstruction of the reference instantaneous spatial distribution of SSI (1280 ×1280 pyranometers at the center of the simulation hour). To retrieve a distribution with an RMSD below 5×10^{-4} compared to the reference, at least 10 pyranometers need to be deployed over

340 1200 s, or alternatively 100 pyranometers over 300 s; the RMSD decrease is mainly controlled by that of the clear-sky mode (Fig. 5(b)). The retrieved distributions shown in Fig. 5(c) confirm that the reference is well captured with such measurement strategies. Interestingly, for long integration times, the RMSD starts increasing, which can be attributed to the non-stationarity of the SSI spatial field, although this non-stationarity does not result in RMSD exceeding 10^{-3} in this ideal simulation.

To summarize this sensitivity study combining observations and simulations, a minimum of 10 pyranometers, uniformly

345 deployed over an area of roughly 10×10 km^2 can capture the instantaneous SSI distribution when integrated for at least 10 min. This means that any such deployment meant to characterize cloud field properties can provide valuable information in a time resolution of roughly 10 minutes. Further research is needed, though, to assess the dependence of the optimal integration time on wind speed.

6   How do SSI distributions change with cloud properties?

350 To illustrate the sensitivity tests presented in Sect. 3.3, Figures 6(a)-(b) show the vertical profiles of LWC and cloud fraction corresponding to one instant of the simulations (51st minute), for each sensitivity test. Figures 6(b)-(i) also show the simulated SSI fields at the same timestep, which further helps understand the modifications made to the cloud fields. Figure 7 and Table 2 present the results of the sensitivity tests in terms of the characteristics of the obtained distributions. In the following, the results are interpreted, with particular emphasis on the 3D effects; note that the highlighted mechanisms might differ for other SZA

355 (here ranging from 34.5 to 36.8° only).

First, we see that increasing cloud LWC (orange solid line in Fig. 7) shifts the cloud-shadow mode towards lower values and the peak in the clear-sky mode towards slightly larger values; this is due to an increase of reflection by cloud sides illustrated by the wider footprint of the white contours in Fig. 6(d) that materialize the 1100 W m^{-2} isoline. However, the largest values (maximum illumination) remain the same as in the original field, suggesting a saturation of 3D effects with LWC. Reducing

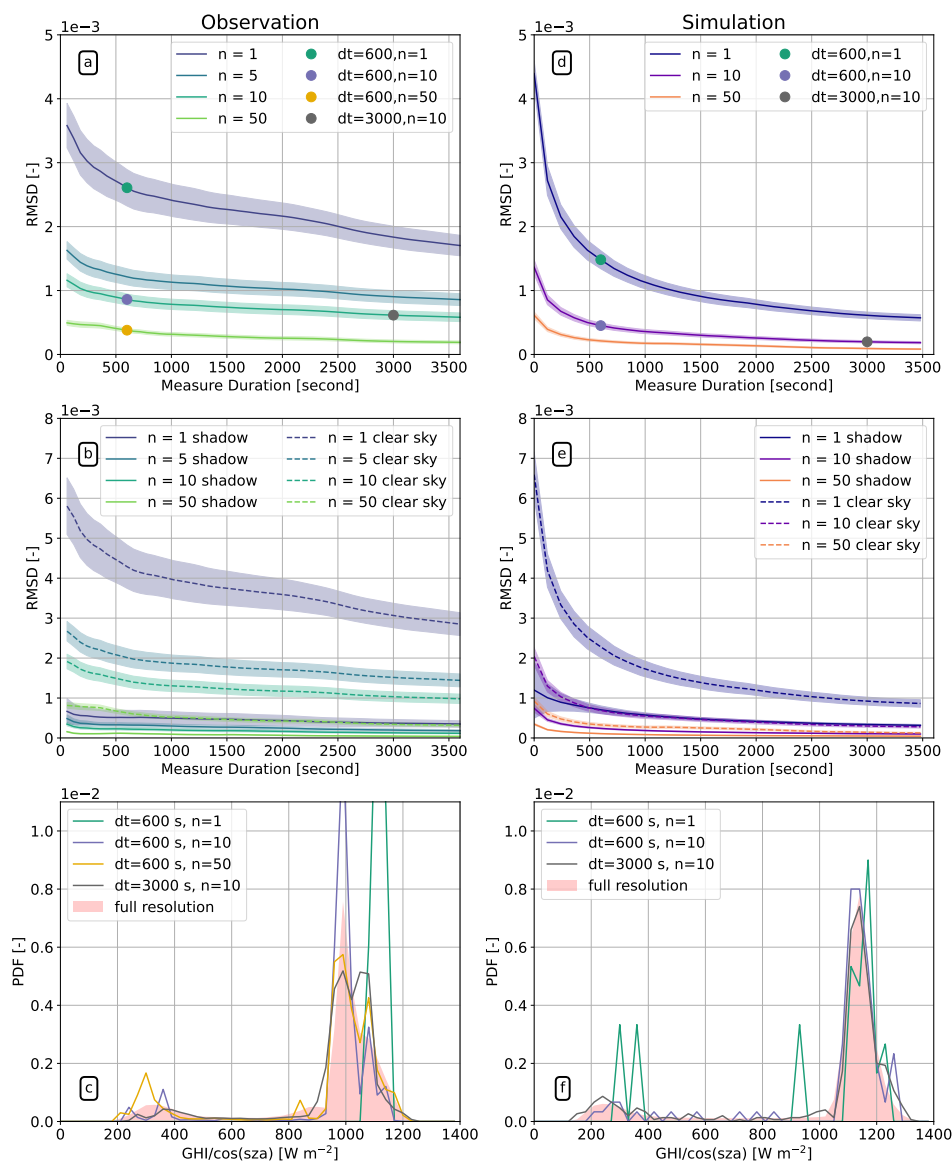360 LWC (orange dashed line) results in the opposite effect.

Figure 4. Spatiotemporal subsampling of the SSI distributions cumulated in observations (P5 period, left column) and simulation (Control, right column). Top row: RMSD with respect to the full distribution as a function of the number of points used for the computation and the cumulative period (x-axis) over which the distribution is computed; the shading indicates ± one standard deviation computed over 512 combinations for a given number of pyranometers and period. Middle row: RMSD computed over the cloud-shadow and the clear-sky modes. Bottom rows: examples of SSI distributions computed from (c) observations and (f) simulations for different numbers of pyranometers and periods; the shading represents the reference simulation computed over 95 pyranometers and cumulated over one hour for the observations and computed over 1280×1280 points and cumulated over one hour for the simulation.
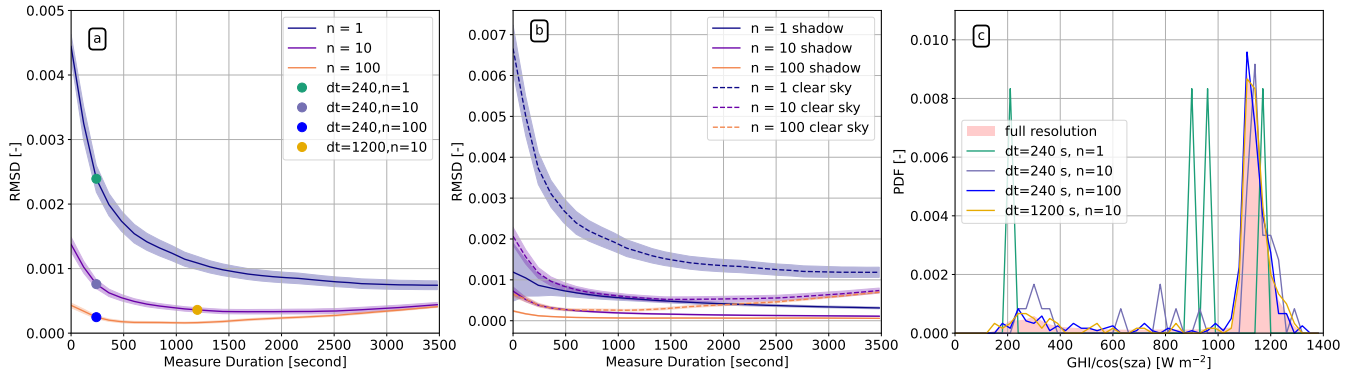
Figure 5. Strategy to measure instantaneous SSI distributions. (a) RMSD with respect to the mid-period instantaneous distribution for simulations as a function of the number of points used and the cumulative period over which the distribution is computed. The shading indicates ± one standard deviation computed over 512 combinations for a given number of points and period. (b) RMSD is computed over the cloud-shadow and the clear-sky modes. (c) Examples of SSI distributions retrieved from different numbers of measurement points. The shading represents the reference distribution computed over 1280×1280 points at a given instant.

Table 2. Summary of the sensitivity tests. All units in $\mathrm{W\,m^{-2}}$, and for normalized SSI, except for the last column (fraction of surface covered by shadow/clear sky) in percent. Here, "shadow" refers to values less than $500\ \mathrm{W\,m^{-2}}$, and "clear-sky" to values greater than $900\ \mathrm{W\,m^{-2}}$. p1 and p99 are respectively the first and 99th percentiles of the distributions.

| Test case	RMSD total/shadow/clear sky $(\times 10^{-4}/\times 10^{-5}/\times 10^{-4})$	mean total/shadow/clear sky	std total/shadow/clear sky	p1/p99	fraction shadow/clear sky
Control	— / — / —	961.0 / 293.8 / 1076.1	269.3 / 82.9 / 49.7	192.9 / 1214.0	12.2 / 82.6
LWCx0.6	4.112 / 9.687 / 6.902	969.2 / 313.7 / 1065.2	240.7 / 84.5 / 49.6	210.6 / 1208.6	9.8 / 84.0
LWCx1.4	2.246 / 6.974 / 3.741	954.9 / 281.5 / 1081.9	285.7 / 80.8 / 48.8	184.9 / 1213.7	13.7 / 81.7
ΔH = −400	7.208 / 10.668 / 12.175	961.0 / 321.0 / 1067.0	254.7 / 83.3 / 61.2	210.0 / 1261.1	11.5 / 83.0
ΔH = 400	3.990 / 7.307 / 6.727	961.6 / 280.3 / 1080.1	275.0 / 84.1 / 43.5	185.6 / 1187.0	12.4 / 82.4
ΔD = 400	6.788 / 14.789 / 11.338	961.1 / 336.5 / 1094.3	28.1 / 23.8 / 5.5	128.6 / 1430.2	12.0 / 77.1
CC = 125	13.703 / 38.865 / 22.876	918.8 / 340.8 / 1136.8	341.2 / 70.5 / 74.3	236.4 / 1301.7	21.8 / 68.1
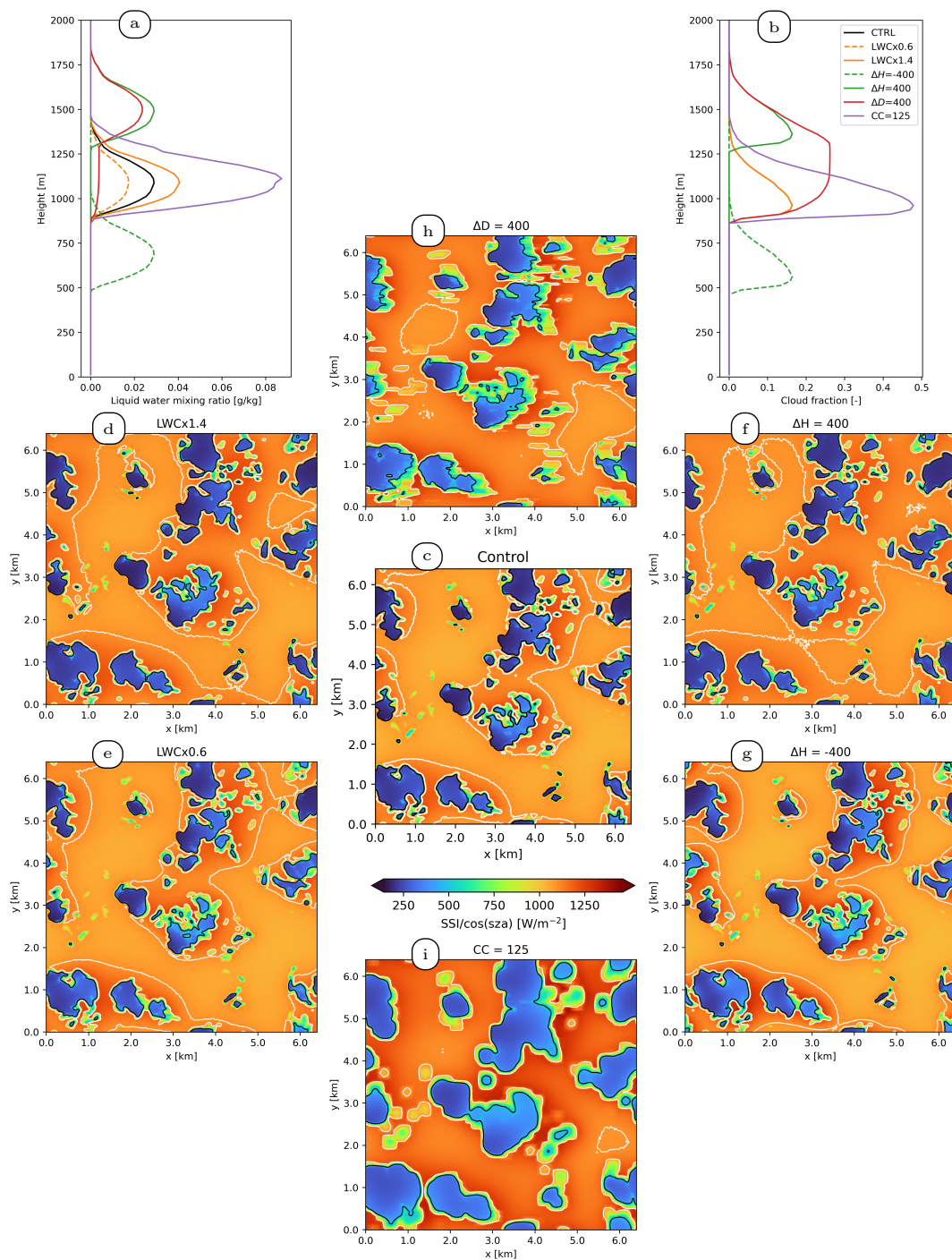
Figure 6. Cloud vertical profiles of (a) LWC and (b) cloud fraction, and SSI fields for control (c) and sensitivity tests (d-i) at minute 51 of the simulation. In the fields, colours represent SSI values, white lines represent the 1100 W m^{-2} isocontour, and black lines represent the 500 W m^{-2} isocontour.
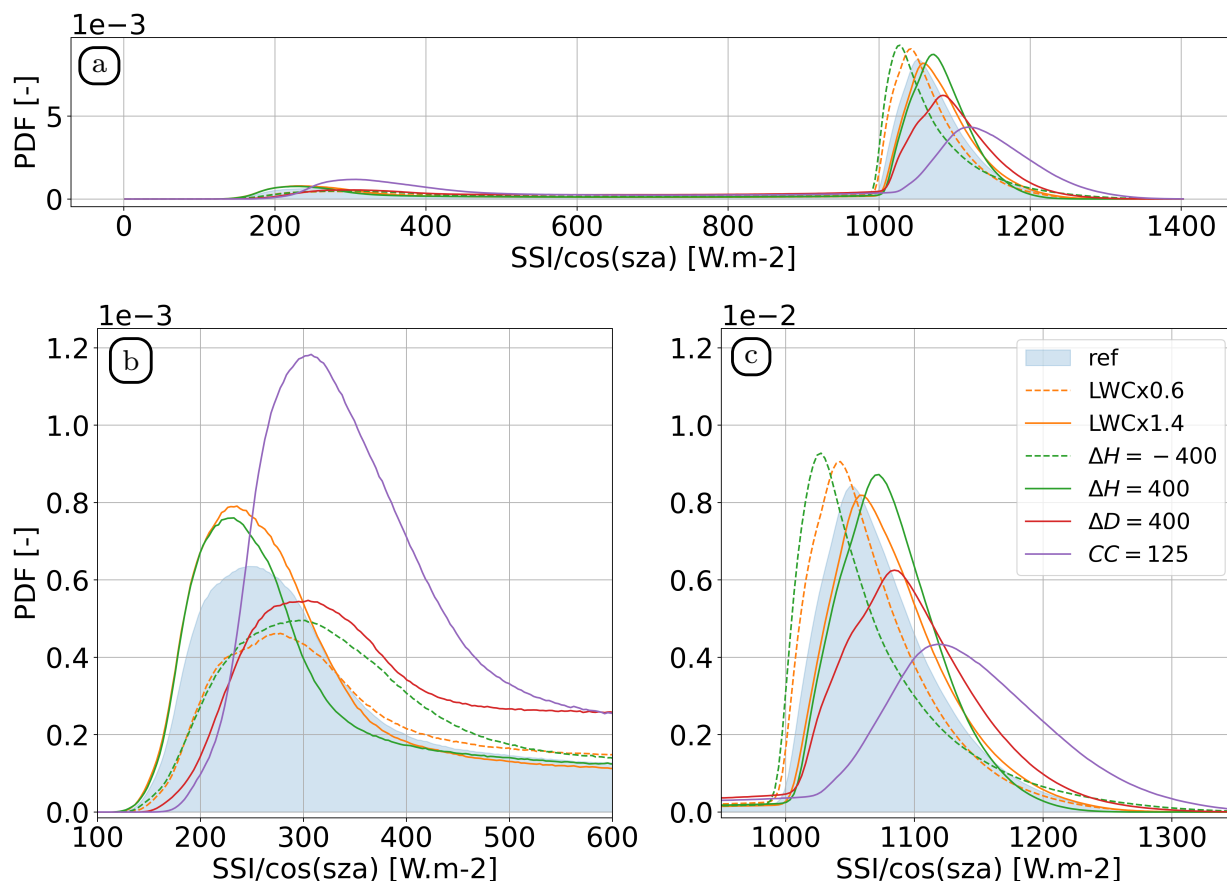
Figure 7. Simulated SSI distributions (a) and zooms over cloud-shadow (b) and clear-sky (c) modes for the various sensitivity tests relative to cloud properties (LWC, cloud base height, cloud depth, and cloud cover). The blue-shaded distribution corresponds to the Control simulation. Distributions were computed using all available data (1280×1280 pixels of size 5 m $\times$ 5m, $times$ 60 minutes), using bins of 3 W m^{-2}. Details regarding the sensitivity tests are given in Table 1.

An increase in cloud base height (solid green line) leads to an increase in the horizontal extension of the footprint of 3D effects (see Fig. 6(f)): as clouds are farther away from the surface, the downwelling diffuse flux can spread farther away from cloud sides before reaching the ground which leads to more directly illuminated pixels affected by neighbohring clouds. Since the radiative flux is spread out horizontally, the maximum illumination is smaller than for lower clouds. Now, if clouds are closer to the surface (green dashed line and Fig. 6(g)), less clear-sky pixels are affected by clouds, but the very localized over-illumination by cloud sides is much more intense. Note that cloud base height modification alone does not change total mean SSI (see Table 2).

When cloud layer depth is increased (red line and Fig. 6(h)), the fraction of shadowed pixels also increases since the shadow cover increases (Várnai and Davies, 1999). As more radiation is intercepted by cloud sides, 3D effects are more intense, and

370 as this extra contribution comes from higher up in the atmosphere, they also have a wider footprint: for any clear-sky pixel, the fraction of visible sky that is occupied by bright, reflecting cloud sides increases with cloud geometrical depth. Shadows are also brighter, as clouds are overall optically thinner to slanted radiation because of the LWC scaling. Note that this modification also leads to the conservation of the mean flux (see Table 2), but for different reasons than cloud height variations: for higher clouds, shadows are darker and clear-sky regions brighter; for deeper clouds, both are brighter, but as clear sky covers a smaller

375 area of the surface, it compensates the overall right-shift of the pdf. This is true throughout the whole simulated hour (not shown); more extensive investigation should be performed to verify if this property is fundamental and remains true for other shifts of height and depth, as well as for other cloud types. Finally, an increase in cloud cover with conservation of the mean in-cloud LWC (hence increasing total LWC in the field) leads to wider shadows and more scattered radiation reaching the surface in clear-sky regions because cloud sides fill a larger portion of the sky, as demonstrated by the right-shift of the clear-sky mode

380 (the distribution becomes dominated by larger SSI values), similar to the case of deeper clouds.

Beyond the detailed modifications of SSI distributions discussed here, these sensitivity tests highlight that the impact of cloud geometrical and physical properties on SSI distributions combines various non-trivial 3D physical processes that make the interpretation much less straightforward than in the common plane-parallel framework. It is important to note that most of the tested modifications would have no significant effect on the SSI distribution under the independent column approximation

385 of radiative transfer, where SSI distributions mostly depend on column-wise liquid water path and vertically projected cloud cover. The consideration of 3D effects is thus necessary to understand the modifications of the distributions and the way they relate to clouds.

7   Conclusions

In this paper, we focused on the instantaneous SSI spatial distribution, an under-explored quantity that is of utmost importance

390 for surface-atmosphere interactions and solar energy applications, especially under broken cloud conditions. We investigated the spatial distribution from both an observational and a numerical perspective. Spatially dense SSI observations from the HOPE field campaign constitute a unique resource to investigate this otherwise barely accessible quantity. By comparing the observed distributions for carefully selected cumulus situations to those simulated with state-of-the-art cloud and 3D radiative transfer modelling, we showed that the numerical simulations are sufficiently reliable to further explore the links between cloud

395 field properties and SSI distributions.

We then investigated how the instantaneous SSI spatial distributions can be estimated using a limited number of pyranometers by taking advantage of cloud motion that allows the sampling of a stationary cloud field from fixed points at the surface. We demonstrated that, for a 10×10 km^2 area, cumulating observations from 10 pyranometers over 10 min can provide the same information on SSI spatial distribution as using 100 pyranometers over a shorter time period. Preliminary tests of optimizing

400 the spatial distribution of the pyranometers indicate that 15 optimized distributed pyranometers can capture the same spatial variability as 100 uniformly distributed pyranometers; this deserves further analysis to understand how this can be deployed

when one does not know in advance the details of the fields that will be observed. This preliminary result paves the way for designing measurement strategies tailored for specific applications related to high-resolution characterization of SSI.

This work is meant to be exploratory and to highlight a poorly known quantity that we believe will become of much more interest to the research community in the coming years as the resolution of numerical weather prediction increases and as observational capabilities for characterizing 3D cloud structure improve. This study confirms that the SSI distribution contains valuable information on cloud properties, including its 3D geometrical properties that most cloud profiling instruments cannot fully capture due to limited spatial sampling. Future work should thus focus on the derivation of relevant cloud properties from a network of pyranometers, which would be a significant step forward for atmospheric sciences. For cumulus situations, the mean and standard deviation of the two peaks of the bimodal SSI distribution seem to provide a wealth of yet unexplored information. This study could also be extended to other campaigns conducted with the pyranometer network. This includes the HOPE dataset acquired near Melpitz, where the network was deployed in a much smaller area of roughly 500×500 m^2, to investigate variability at even smaller scales. Recently, the network was deployed in the framework of the Small-Scale Variability of Solar Radiation campaign (S2VSR), which was conducted at the ARM Southern Great Plains site and targeted an area of 6 x 6 km^2. Although the dataset was not yet available at the start of this investigation, several ancillary observations are available based on routine ARM measurements, which can help further understand factors influencing the SSI distribution. Calibration/validation campaigns are also planned for the upcoming launch of the EarthCARE satellite mission, where small-scale radiative closure experiments will be carried out and would benefit from such an instrumental deployment.

The fact that SSI distributions are so tightly related to most 3D thermodynamical properties of the atmosphere also offers an advanced framework for evaluating LES in a much more stringent way than currently done when LES properties are generally spatially averaged to be compared to vertical profiles at well-instrumented sites. In particular, we believe that the correct representation of LWC and cloud droplet effective radius heterogeneity, which currently represents a challenge for LES, could be tackled with such observations. Relying on the objective determination of cumulus cloud conditions set up in this study, we also encourage the development of cloud classifications based on SSI observations, using, for instance, the metrics introduced in this study. Such classifications could be used for comparison of cloud conditions at different sites or to study the variability of weather conditions in a much more robust way than human-based classifications. These diverse perspectives highlight the potential of considering SSI spatial distributions and suggest that in the future, networks of radiation sensors should be more systematically deployed during field campaigns dedicated to boundary layer clouds and surface-atmosphere interactions.

Data availability

Simulation data supporting our results are available on Zenodo (He et al., 2024). The repository includes radiative transfer simulation outputs, scripts to launch radiative transfer simulations with htrdr version 0.8.1 (https://www.meso-star.com/projects/htrdr/htrdr.html, source code also in the archive) and to reproduce tables and figures, as well as namelists to run Large-Eddy Simulations with the community code Meso-NH, version 5.4.3 (http://mesonh.aero.obs-mip.fr/mesonh/dir_open/

dir_MESONH/MNH-V5-4-3.tar.gz). It does not include Large Eddy Simulation 3D output fields but they will be provided on
435 demand. Observational data is available at re3data (Registry of Research Data Repositories., 2017; Bomidi, 2022).

Author contribution

ZH, NV, QL and FC analysed the data; NV, FC and ZH performed the simulations; QL, FC, NV and ZH wrote the manuscript
draft; HD and JW reviewed and edited the manuscript.

Competing interests

440 The authors declare that they have no conflict of interest.

References

Alam, M., Muttaqi, K., and Sutanto, D.: A novel approach for ramp-rate control of solar PV using energy storage to mitigate output fluctuations caused by cloud passing, IEEE Transactions on Energy Conversion, 29, 507–518, 2014.

Berg, L. K., Kassianov, E. I., Long, C. N., and L., M. D.: Surface summertime radiative forcing by shallow cumuli at the Atmospheric Radiation Measurement Southern Great Plains site, J. Geophys. Res., 116, https://doi.org/10.1029/2010JD014593, 2011.

Beyer, H. G.: Handling of small scale structures of the irradiance field for solar energy system analysis–a review, Energy Procedia, 97, 141–148, 2016.

Bomidi, M.: HD(CP)2 short term observations, sw broadband downwelling radiation (surface) data of Pyranometer network (no. 00), HOPE campaign by TROPOS, data version 00, pID: de.koeln.rrzk/amd.de.hope/trop.pyrnet00.l1.rsds, 2022.

Brown, A., Cederwall, R. T., Chlond, A., Duynkerke, P. G., Golaz, J.-C., Khairoutdinov, M., Lewellen, D., Lock, A., MacVean, M., Moeng, C.-H., et al.: Large-eddy simulation of the diurnal cycle of shallow cumulus convection over land, Quarterly Journal of the Royal Meteorological Society: A journal of the atmospheric sciences, applied meteorology and physical oceanography, 128, 1075–1093, 2002.

Bühl, J., Seifert, P., Wandinger, U., Baars, H., Kanitz, T., Schmidt, J., Myagkov, A., Engelmann, R., Skupin, A., Heese, B., Klepel, A., Althausen, D., and Ansmann, A.: LACROS: the Leipzig Aerosol and Cloud Remote Observations System, in: Remote Sensing of Clouds and the Atmosphere XVIII; and Optics in Atmospheric Propagation and Adaptive Systems XVI, edited by Comeron, A., Kassianov, E. I., Schäfer, K., Stein, K., and Gonglewski, J. D., vol. 8890, p. 889002, International Society for Optics and Photonics, SPIE, https://doi.org/10.1117/12.2030911, 2013.

Cahalan, R. F., Oreopoulos, L., Marshak, A., Evans, K. F., Davis, A. B., Pincus, R., Yetzer, K. H., Mayer, B., Davies, R., Ackerman, T. P., Barker, H. W., Clothiaux, E. E., Ellingson, R. G., Garay, M. J., Kassianov, E., Kinne, S., Macke, A., O'Hirok, W., Partain, P. T., Prigarin, S. M., Rublev, A. N., Stephens, G. L., Szczap, F., Takara, E. E., Várnai, T., Wen, G., and Zhuravleva, T. B.: The I3RC: Bringing Together the Most Advanced Radiative Transfer Tools for Cloudy Atmospheres, Bulletin of the American Meteorological Society, 86, 1275–1293, https://doi.org/10.1175/BAMS-86-9-1275, 2005.

Cuxart, J., Bougeault, P., and Redelsperger, J.-L.: A turbulence scheme allowing for mesoscale and large-eddy simulations, Quarterly Journal of the Royal Meteorological Society, 126, 1–30, http://doi.wiley.com/10.1002/qj.49712656202, 2000.

de Andrade, R. C. and Tiba, C.: Extreme global solar irradiance due to cloud enhancement in northeastern Brazil, Renewable energy, 86, 1433–1441, 2016.

Deardorff, J. W.: Stratocumulus-capped mixed layers derived from a three-dimensional model, Boundary-Layer Meteorology, 18, 495–527, https://doi.org/10.1007/BF00119502, 1980.

Emck, P. and Richter, M.: An upper threshold of enhanced global shortwave irradiance in the troposphere derived from field measurements in tropical mountains, Journal of Applied Meteorology and Climatology, 47, 2828–2845, 2008.

Endo, S., Zhang, ., Vogelmann, A. M., Kollias, P., Lamer, K., Oue, M., Xiao, H., Gustafson, W. I., and Romps, D. M.: Reconciling Differences Between Large-Eddy Simulations and Doppler Lidar Observations of Continental Shallow Cumulus Cloud-Base Vertical Velocity, Geophys. Res. Lett., 46, 11 539–11 544, https://doi.org/10.1029/2019GL084893, 2019.

Gristey, J. J., Feingold, G., Glenn, I. B., Schmidt, K. S., and Chen, H.: On the relationship between shallow cumulus cloud field properties and surface solar irradiance, Geophysical Research Letters, 47, e2020GL090 152, 2020a.

Gristey, J. J., Feingold, G., Glenn, I. B., Schmidt, K. S., and Chen, H.: Surface solar irradiance in continental shallow cumulus fields: Observations and large-eddy simulation, Journal of the Atmospheric Sciences, 77, 1065–1080, 2020b.

480 Gueymard, C. A.: Cloud and albedo enhancement impacts on solar irradiance using high-frequency measurements from thermopile and photodiode radiometers. Part 1: Impacts on global horizontal irradiance, Solar Energy, 153, 755–765, 2017.

Gustafson Jr, W. I., Vogelmann, A. M., Li, Z., Cheng, X., Dumas, K. K., Endo, S., Johnson, K. L., Krishna, B., Fairless, T., and Xiao, H.: The large-eddy simulation (LES) atmospheric radiation measurement (ARM) symbiotic simulation and observation (LASSO) activity for continental shallow convection, Bulletin of the American Meteorological Society, 101, E462–E479, 2020.

485 He, Z., Libois, Q., Villefranque, N., Deneke, H., Witthuhn, J., and Couvreux, F.: How to observe the small-scale spatial distribution of surface solar irradiance, and how is it influenced by cumulus clouds?, https://doi.org/10.5281/zenodo.10948325., 2024.

Hogan, R. J., Fielding, M. D., Barker, H. W., Villefranque, N., and Schäfer, S. A. K.: Entrapment: An Important Mechanism to Explain the Shortwave 3D Radiative Effect of Clouds, Journal of the Atmospheric Sciences, 76, 2123–2141, https://doi.org/10.1175/JAS-D-18-0366.1, 2019.

490 Holmgren, W. F., Hansen, C. W., and Mikofski, M. A.: pvlib python: A python package for modeling solar energy systems, Journal of Open Source Software, 3, 884, 2018.

Huang, G., Li, Z., Li, X., Liang, S., Yang, K., Wang, D., and Zhang, Y.: Estimating surface solar irradiance from satellites: Past, present, and future perspectives, Remote Sensing of Environment, 233, 111 371, 2019.

Iacono, M. J., Delamere, J. S., Mlawer, E. J., Shephard, M. W., Clough, S. A., and Collins, W. D.: Radiative forcing by long-
495   lived greenhouse gases: Calculations with the AER radiative transfer models, Journal of Geophysical Research: Atmospheres, 113, https://doi.org/10.1029/2008JD009944, 2008.

Ineichen, P.: A broadband simplified version of the Solis clear sky model, Solar Energy, 82, 758–762, 2008.

Ineichen, P.: Validation of models that estimate the clear sky global and beam solar irradiance, Solar Energy, 132, 332–344, 2016.

Inman, R. H., Chu, Y., and Coimbra, C. F.: Cloud enhancement of global horizontal irradiance in California and Hawaii, Solar Energy, 130,
500   128–138, 2016.

Jakub, F. and Mayer, B.: The role of 1-D and 3-D radiative heating in the organization of shallow cumulus convection and the formation of cloud streets, Atmospheric Chemistry and Physics, 17, 13 317–13 327, 2017.

Kuhn, P., Wilbert, S., Prahl, C., Schüler, D., Haase, T., Hirsch, T., Wittmann, M., Ramirez, L., Zarzalejo, L., Meyer, A., et al.: Shadow camera system for the generation of solar irradiance maps, Solar Energy, 157, 157–170, 2017.

505 Lac, C., Chaboureau, J.-P., Masson, V., Pinty, J.-P., Tulet, P., Escobar, J., Leriche, M., Barthe, C., Aouizerats, B., Augros, C., Aumond, P., Auguste, F., Bechtold, P., Berthet, S., Bielli, S., Bosseur, F., Caumont, O., Cohard, J.-M., Colin, J., Couvreux, F., Cuxart, J., Delautier, G., Dauhut, T., Ducrocq, V., Filippi, J.-B., Gazen, D., Geoffroy, O., Gheusi, F., Honnert, R., Lafore, J.-P., Lebeaupin Brossier, C., Libois, Q., Lunet, T., Mari, C., Maric, T., Mascart, P., Mogé, M., Molinié, G., Nuissier, O., Pantillon, F., Peyrillé, P., Pergaud, J., Perraud, E., Pianezze, J., Redelsperger, J.-L., Ricard, D., Richard, E., Riette, S., Rodier, Q., Schoetter, R., Seyfried, L., Stein, J., Suhre, K., Taufour,
510   M., Thouron, O., Turner, S., Verrelle, A., Vié, B., Visentin, F., Vionnet, V., and Wautelet, P.: Overview of the Meso-NH model version 5.4 and its applications, Geoscientific Model Development, 11, 1929–1969, https://doi.org/10.5194/gmd-72811-1929-2018, 2018.

Lappalainen, K. and Kleissl, J.: Analysis of the cloud enhancement phenomenon and its effects on photovoltaic generators based on cloud speed sensor measurements, Journal of Renewable and Sustainable Energy, 12, 2020.

Lindsay, N., Libois, Q., Badosa, J., Migan-Dubois, A., and Bourdin, V.: Errors in PV power modelling due to the lack of spectral and angular
515   details of solar irradiance inputs, Solar Energy, 197, 266–278, 2020.

Lohmann, G. M.: Irradiance variability quantification and small-scale averaging in space and time: A short review, Atmosphere, 9, 264, 2018.

Lohmann, G. M. and Monahan, A. H.: Effects of temporal averaging on short-term irradiance variability under mixed sky conditions, Atmospheric measurement techniques, 11, 3131–3144, 2018.

Lohmann, G. M., Monahan, A. H., and Heinemann, D.: Local short-term variability in solar irradiance, Atmospheric chemistry and physics, 520   16, 6365–6379, 2016.

Lohou, F. and Patton, E. G.: Surface energy balance and buoyancy response to shallow cumulus shading, Journal of the Atmospheric Sciences, 71, 665–682, 2014.

Long, C. N., Ackerman, T. P., Gaustad, K. L., and Cole, J.: Estimation of fractional sky cover from broadband shortwave radiometer measurements, Journal of Geophysical Research: Atmospheres, 111, 2006.

525   Luger, S., Mock, J., Zehner, M., Lorenz, E., Kühnert, J., Weigl, T., Nagl, L., Rauscher, T., Becker, G., Betts, T. R., and Gottschalg, R.: 3D-SIM (3D-Solar Irradiance Modelling): The Optimization of An Irradiance-Interpolation-Method and its Application for Central Europe, https://api.semanticscholar.org/CorpusID:131240813, 2013.

Macke, A., Seifert, P., Baars, H., Barthlott, C., Beekmans, C., Behrendt, A., Bohn, B., Brueck, M., Bühl, J., Crewell, S., et al.: The HD (CP) 2 observational prototype experiment (HOPE)–An overview, Atmospheric chemistry and physics, 17, 4887–4914, 2017.

530   Madhavan, B. L., Kalisch, J., and Macke, A.: Shortwave surface radiation network for observing small-scale cloud inhomogeneity fields, Atmospheric Measurement Techniques, 9, 1153–1166, 2016.

Madhavan, B. L., Deneke, H., Witthuhn, J., and Macke, A.: Multiresolution analysis of the spatiotemporal variability in global radiation observed by a dense network of 99 pyranometers, Atmospheric Chemistry and Physics, 17, 3317–3338, 2017.

Marshak, A. and Davis, A., eds.: 3D Radiative Transfer in Cloudy Atmospheres, Physics of Earth and Space Environments, Springer-Verlag, 535   Berlin Heidelberg, ISBN 978-3-540-23958-1, dOI: 10.1007/3-540-28519-9, 2005.

Meso-Star: htrdr atmosphere starter pack v0.7, https://www.meso-star.com/projects/htrdr/htrdr-atmosphere-spk.html, dataset, 2021.

Mishchenko, M., D. Travis, L., and Lacis, A.: Scattering, Absorption, and Emission of Light by Small Particles, vol. 4, 2002.

Mol, W., Heusinkveld, B., Mangan, M., Hartogensis, O., Veerman, M., and Heerwaarden, C. v.: Observed Patterns of Surface Solar Irradiance under Cloudy and Clear-sky Conditions, 2023.

540   Neggers, R. A. J., G., D. P., and Rodts, S. M. A.: Shallow cumulus convection: a validation of large-eddy simulation against aircraft and Landsat observations, Quart. J. Roy. Meteorol. Soc., 129, 2671–2696, https://doi.org/10.1256/qj.02.93, 2003.

Nouri, B., Wilbert, S., Segura, L., Kuhn, P., Hanrieder, N., Kazantzidis, A., Schmidt, T., Zarzalejo, L., Blanc, P., and Pitz-Paal, R.: Determination of cloud transmittance for all sky imager based solar nowcasting, Solar Energy, 181, 251–263, 2019.

Nouri, B., Blum, N., Wilbert, S., and Zarzalejo, L. F.: A hybrid solar irradiance nowcasting approach: Combining all sky imager systems and 545   persistence irradiance models for increased accuracy, Solar RRL, 6, 2100 442, 2022.

Oue, M., P., K., North, K. W., A., T., S., E., M, V. A., and I., G. W.: Estimation of cloud fraction profile in shallow convection using a scanning cloud radar, Geophys. Res. Lett., 43, 10 998–11 006, https://doi.org/10.1002/2016GL070776, 2016.

Pacifici, M., Rama, F., and de Castro Marins, K. R.: Analysis of temperature variability within outdoor urban spaces at multiple scales, Urban Climate, 27, 90–104, 2019.

550   Pinty, J.-P. and Jabouille, P.: A mixed-phase cloud parameterization for use in mesoscale non-hydrostatic model: simulations of a squall line and of orographic precipitations, Proceedings of the conference on cloud physics, pp. 217–220, 1998.

Qu, Z., Oumbe, A., Blanc, P., Espinar, B., Gesell, G., GSCHwIND, B., Klüser, L., Lefèvre, M., Saboret, L., Schroedter-Homscheidt, M., et al.: Fast radiative transfer parameterisation for assessing the surface solar irradiance: The Heliosat-4 method, Meteorologische Zeitschrift, 26, 33–57, 2017.

555 Registry of Research Data Repositories.: SAMD, https://doi.org/10.17616/R3D944, last accessed: 2024-04-08; editing status 2023-08-29, 2017.

Sanchez, B., Roth, M., Simón-Moral, A., Martilli, A., and Velasco, E.: Assessment of a meteorological mesoscale model's capability to simulate intra-urban thermal variability in a tropical city, Urban Climate, 40, 101 006, 2021.

Sengupta, M. and Andreas, A.: Oahu solar measurement grid (1-year archive): 1-second solar irradiance; Oahu, Hawaii (data), 2010.

560 Siebesma, A. P., Bretherton, C. S., Brown, A., Chlond, A., Cuxart, J., Duynkerke, P. G., Jiang, H., Khairoutdinov, M., Lewellen, D., Moeng, C.-H., et al.: A large eddy simulation intercomparison study of shallow cumulus convection, Journal of the Atmospheric Sciences, 60, 1201–1219, 2003.

Tabar, M. R. R., Anvari, M., Lohmann, G., Heinemann, D., Wächter, M., Milan, P., Lorenz, E., and Peinke, J.: Kolmogorov spectrum of renewable wind and solar power fluctuations, The European Physical Journal Special Topics, 223, 2637–2644, 2014.

565 Tijhuis, M., van Stratum, B. J., Veerman, M. A., and van Heerwaarden, C. C.: An Efficient Parameterization for Surface Shortwave 3D Radiative Effects in Large-Eddy Simulations of Shallow Cumulus Clouds, Journal of Advances in Modeling Earth Systems, 15, e2022MS003 262, 2023.

Várnai, T. and Davies, R.: Effects of cloud heterogeneities on shortwave radiation: Comparison of cloud-top variability and internal heterogeneity, Journal of the atmospheric sciences, 56, 4206–4224, 1999.

570 Veerman, M., van Stratum, B., and van Heerwaarden, C.: A case study of cumulus convection over land in cloud-resolving simulations with a coupled ray tracer, Geophysical Research Letters, p. e2022GL100808, 2022.

Villefranque, N. and Hogan, R. J.: Evidence for the 3D Radiative Effects of Boundary-Layer Clouds From Observations of Direct and Diffuse Surface Solar Fluxes, Geophysical Research Letters, 48, e2021GL093 369, 2021.

Villefranque, N., Fournier, R., Couvreux, F., Blanco, S., Cornet, C., Eymet, V., Forest, V., and Tregan, J.-M.: A Path-Tracing Monte Carlo 575 Library for 3-D Radiative Transfer in Highly Resolved Cloudy Atmospheres, Journal of Advances in Modeling Earth Systems, 11, 2449– 2473, 2019.

Villefranque, N., Barker, H. W., Cole, J. N. S., and Qu, Z.: A Functionalized Monte Carlo 3D Radiative Transfer Model: Radiative Effects of Clouds Over Reflecting Surfaces, Journal of Advances in Modeling Earth Systems, 15, e2023MS003 674, https://doi.org/https://doi.org/10.1029/2023MS003674, e2023MS003674 2023MS003674, 2023.

580 Weigl, T., Nagl, L., Weizenbeck, J., Zehner, M., Augel, M., Giesler, B., Becker, G., Mayer, O., Betts, T., and Gottschalg, R.: Modelling and Validation of Spatial Irradiance Characteristics for Localised Irradiance Fluctuations and Enhancements, https://doi.org/10.4229/27thEUPVSEC2012-5CO.7.6, 2012.

Yordanov, G. H., Midtgård, O.-M., Saetre, T. O., Nielsen, H. K., and Norum, L. E.: Overirradiance (cloud enhancement) events at high latitudes, in: 2012 IEEE 38th photovoltaic specialists conference (PVSC) part 2, pp. 1–7, IEEE, 2012.